Journal of Physics: Energy

PAPER

Structural analyses and photovoltaic device simulations in two and three dimensions applied to Ag-alloyed Cu(In,Ga)Se_2 solar cells

Chang-Yun Song[1,*], **Zelong Wang**[2], **Matthias Maiberg**[1], **Heiko Kempa**[1], **Julia Horstmann**[1], **Wolfram Witte**[3], **Rico Gutzler**[3], **Dimitrios Hariskos**[3], **Daniel Abou-Ras**[4], **Sinju Thomas**[4], **Roland Scheer**[1] and **Ali Gholinia**[2]

[1] Institute of Physics, Martin Luther University Halle-Wittenberg, Von-Danckelmann-Platz 3, 06120 Halle (Saale), Germany
[2] Department of Materials and Henry Royce Institute, The University of Manchester, Manchester M13 9PL, United Kingdom
[3] Zentrum für Sonnenenergie- und Wasserstoff-Forschung Baden-Württemberg (ZSW), Meitnerstr. 1, 70563 Stuttgart, Germany
[4] Helmholtz-Zentrum Berlin für Materialien und Energie GmbH, Hahn-Meitner-Platz 1, 14109 Berlin, Germany
[*] Author to whom any correspondence should be addressed.

E-mail: chang-yun.song@physik.uni-halle.de

OPEN ACCESS

RECEIVED
10 April 2025

REVISED
26 May 2025

ACCEPTED FOR PUBLICATION
29 May 2025

PUBLISHED
9 June 2025

Keywords: 3D EBSD, microstructure analysis, grain boundaries, device simulation, Ag alloying, Cu(In, Ga)Se_2 solar cells

Supplementary material for this article is available online

Abstract

The present study reports on the structural changes and related photovoltaic properties resulting from the addition of Ag in Cu(In,Ga)Se_2 (CIGS)-based thin-film solar cells analysed using two-dimensional (2D) and three-dimensional (3D) analytical and modelling techniques. The microstructures of CIGS and Ag-containing CIGS (ACIGS) layers were characterized by means of 2D and 3D electron backscatter diffraction (EBSD). Ag addition significantly increased grain sizes, which is differently observed in the 2D and 3D EBSD analyses due to the different methodology. Moreover, opto-electronic 3D device simulations, which incorporate real 3D structural data obtained from 3D EBSD, confirmed that 2D models tend to underestimate the impact of grain boundaries on the device performance. Device simulations showed that the increased grain size and thus, the decreased grain-boundary density, resulting from Ag addition had a positive effect on the open-circuit voltage (V_{OC}) of the solar cell. The V_{OC} improvement was more pronounced in ACIGS layers of high minority-carrier lifetimes. These findings highlight the necessity of combining 3D EBSD analysis with 3D device simulations to optimize the relationship between microstructural characteristics and photovoltaic performance in solar cells to understand opto-electronic properties more quantitatively.

1. Introduction

Thin-film solar cells based on polycrystalline Cu(In,Ga)Se_2 (CIGS) absorber layers have attracted significant commercial interest as a highly promising renewable energy source owing to their high energy conversion efficiencies and excellent long-term stability [1–3]. Particularly, this technology occupies a crucial position in the field of solar energy due to its high absorption coefficient and exceptional photovoltaic efficiency [4]. However, the performance of CIGS solar cells is often constrained by the polycrystalline nature of their structure, notably at the grain boundaries (GBs), which facilitate charge carrier recombination, thereby reducing the overall conversion efficiencies of the devices [5–7].

To address this issue, recent studies demonstrated that the addition of Ag can influence significantly the micro structure and the average grain size of CIGS thin films [8–11]. Doping with Ag has been shown to enlarge crystal grains and reduce grain boundary densities, potentially decreasing the likelihood of charge carrier recombination. Furthermore, CIGS films with added Ag maintain high performance even at low growth temperatures, enhancing the flexibility of the manufacturing process and reducing production costs [3, 12, 13]. Furthermore, Ag affects not only the fabrication process and grain structure but also the electrical

properties. Depending on the Ag content, the bandgap can be tuned from 1.0 eV to 1.8 eV, providing a wider bandgap range than that achievable with conventional Ag-free CIGS [14–20]. Additionally, Ag incorporation can shift the band edges, allowing for control of band alignments and band offsets with adjacent layers, which is crucial for optimizing charge transport and minimizing recombination losses [21]. Moreover, at low Ag substitution levels, the addition of Ag increases carrier lifetime and mobility while decreasing the doping density [22, 23].

So far, most studies on CIGS and other types of solar cells have relied on two-dimensional (2D) analytical techniques, which are limited in their ability to capture fully the complex three-dimensional (3D) structures within the devices [24, 25]. In this paper we present advanced 3D analytical techniques which we employed to precisely analyse the grain structure of Ag-added CIGS thin films and to compare these findings with traditional 2D analysis results. We employed 3D electron backscatter diffraction (EBSD) analysis and device simulations to show how Ag-induced changes in microstructure affect the photovoltaic properties. By means of this integrated approach, we provide new insights into optimizing the design and performance of next-generation thin-film solar cells, including tandem solar cells [12, 26–28].

2. Sample preparation and analytical approach

2.1. Sample preparation

CIGS and silver-alloyed CIGS (ACIGS) thin films were prepared on molybdenum-coated alkali-containing glass substrates using a three-stage co-evaporation process [29, 30] or an in-line multi-stage co evaporation process [10]. The CIGS absorber layer had a thickness of approximately 2.8 μm, and the [Ga]/([Ga]+[In]) ratio (GGI) was kept 0.35. To further optimize the absorber properties, CsF post-deposition treatment (PDT) was performed under a selenium atmosphere [31].

For the ACIGS absorber layer, Ag was incorporated directly during deposition without the use of precursors resulting in an [Ag]/([Ag]+[Cu]) ratio (AAC) of 0.07. The absorber thickness was approximately 2.1 μm, and the GGI was 0.28, and *in-situ* RbF-PDT was applied at the end of the in-line process under selenium atmosphere [10]. For both CIGS and ACIGS a solution-grown CdS buffer layer was deposited on the absorbers. Transparent conductive layers were then added by sputtering. ZnMgO and ZnO:Al layers were used for CIGS devices, while ZnO and ZnO:Al layers were used for ACIGS devices. A Ni/Al/Ni grid was added to both device types to ensure reliable electrical contacts. The cells had a total area of 0.5 cm^2 and contained no anti-reflective coating.

2.2. Analytical approach

Microstructural and crystallographic properties, including grain size, orientation, and grain boundary density, were analysed using 2D and 3D EBSD techniques. 2D analyses were conducted on in-plane and on cross-sectional planes, while 3D analysis utilized focused ion beam (FIB) serial sectioning for reconstructing grain structures. Measurements were performed with the Helios™ 5 Laser PFIB system (Thermo Scientific) [32, 33]. The 3D EBSD datasets consisted of each 80 individual EBSD maps. Between each 2D EBSD measurement, a slice with a thickness of about 50 nm was sectioned using a Xe plasma ion beam (30 kV, 15 nA).

The EBSD mapping was conducted at 20 kV and 1.6 nA beam current. For the CIGS sample, a 200 pixel × 200 pixel area was covered at a step size of 50 nm. For the ACIGS sample, the same slicing and mapping conditions were applied, but the mapping area was extended to 400 pixel × 400 pixels to account for the larger average grain size. Both samples achieved an indexing success rate of over 70%, and the data were processed using AZtec and AZtecCrystal software (Oxford Instruments). The EBSD data were used to reconstruct 3D grain structures and evaluate grain size, shape, and local crystal orientation.

3. Result and discussion

3.1. Microstructure analysis of CIGS and ACIGS thin films using EBSD

To investigate the grain morphology and grain size of CIGS and ACIGS samples, EBSD measurements were performed as shown in figure 1, classifying grains based on their crystallographic orientations. In order to obtain microstructural insights in 3D, 2D EBSD maps were acquired in plan-view configuration at various depths (alternatingly measuring EBSD maps and removing material using a FIB) to generate a stack of 2D EBSD maps, which was subsequently reconstructed into a 3D EBSD data cube (a multi-dimensional data structure storing crystallographic features in 3D space) [33, 34]. Figures 1(a) and (b) show 2D EBSD maps acquired in plan-view on CIGS and ACIGS layers, both at a depth of about 1 μm. It is apparent that the ACIGS layer (figure 1(b)) reveals larger grain sizes at the same depth. EBSD maps measured on cross-sections of these thin films (figures 1(c) and (d)) corroborate this finding. In figure 1(c), the CIGS layer

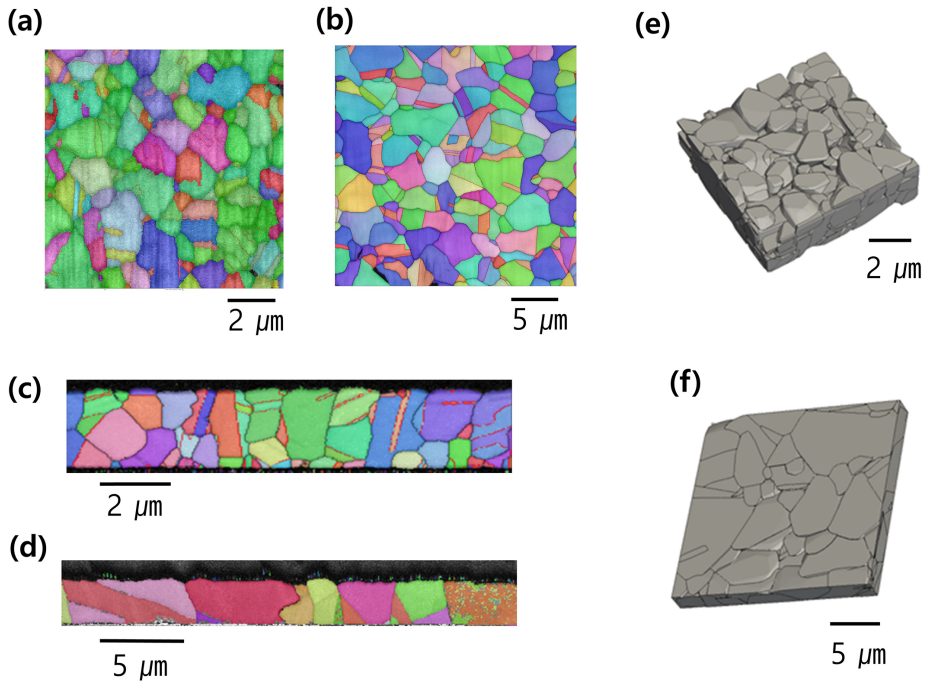

Figure 1. EBSD analysis and 3D reconstructed models of CIGS and ACIGS samples (note the different scale bars). (a) and (b) show the EBSD in-plane images of CIGS and ACIGS, respectively, measured at a depth of 1 μm, with ACIGS exhibiting larger grain sizes. (c) and (d) are EBSD cross-sectional images, illustrating the effect of Ag addition along the z-axis. (e) and (f) represent 3D reconstructed grain models, depicting the grain structures of CIGS and ACIGS, respectively.

exhibits a gradient in grain size perpendicular to the substrate, with smaller grains near the back contact and larger grains toward the surface. This variation is strongly influenced by the Ga/In chemical composition ratio perpendicular to the substrate (figure S1). $CuInSe_2$ tends to form larger grains compared with $CuGaSe_2$ owing to its lower (absolute) formation energy, leaving more residual energy for grain growth that is, energy that can promote grain boundary migration and coalescence [35–37]. Additionally, the tetragonal crystal structure of $CuInSe_2$ exhibits a lattice-constant ratio c/a that deviates less from the pseudocubic value ($c\,a^{-1} = 2$), leading to reduced microstrain compared with the crystal structure of $CuGaSe_2$ [38–41]. Due to the significant difference in bond lengths between In–Se and Cu–Se, In atoms tend to segregate towards the surface during film growth [42, 43]. This surface enrichment leads to a higher local concentration of $CuInSe_2$ near the top of the absorber, where grain growth is more favourable, thereby contributing to the observed grain size gradient.

In contrast, figure 1(d) shows that the ACIGS layer exhibits significantly larger and more contiguous grain structures across the entire thickness of the film. Unlike CIGS, which features a noticeable grain size gradient, the ACIGS sample maintains consistently large grains throughout the entire film thickness, despite having a similar Ga gradient (figure S1). This effect is attributed to Ag incorporation. The formation energy of $AgInSe_2$ is smaller than that of $CuInSe_2$ (in absolute terms), leading to enhanced grain growth (at same deposition temperatures) and promoting grain coalescence by modifying the bonding environment and reducing microstrain in the ACIGS film, provided that the Ag content is not excessively high [9, 37, 44, 45]. Figures 1(e) and (f) show the 3D EBSD data cubes of CIGS and ACIGS reconstructed from the 2D EBSD stacks. For further details on the reconstruction process, the reader is referred to [41]. These 3D reconstructions incorporate the information visible in both the plan-view and cross-sectional analyses, while providing additional insights that cannot be obtained from 2D analysis alone, such as grain volume, surface area, and morphology [24, 46, 47].

To quantitatively the analyse grain size distributions in each layer, histograms of grain sizes obtained by corresponding 2D and 3D analyses were calculated (figure 2). In the 2D data, grain size was measured based on the equivalent circle diameter, while the 3D data used the equivalent sphere diameter. Due to grain size variations caused by Ga/In gradients through the film thickness, cross-sectional EBSD analysis is a commonly used approach. Figures 2(a) and (d) give the grain size distributions as obtained from one EBSD cross section view. These grain size distributions of the Ag-free (a) and Ag-doped (d) samples illustrate the significant increase in median grain size due to Ag addition, from 0.29 μm in CIGS to 0.71 μm in ACIGS, representing approximately a 2.5 times increase. Subsequently, EBSD measurements were conducted on all

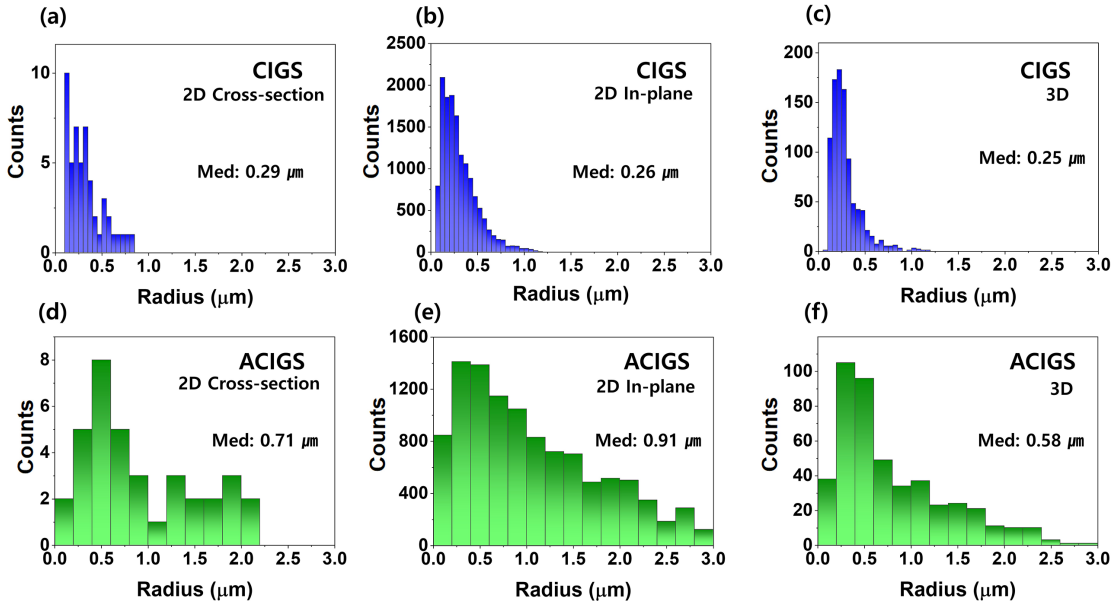

Figure 2. Histograms of grain size distributions for CIGS and ACIGS samples were analysed using 2D cross sectional view, 2D in-plane-view, and 3D methods. (a)–(c) Show results for CIGS, and (d)–(f) show results for ACIGS. (a) And (d) are 2D cross section-view data, (b) and (e) are 2D in-plane data, and (c) and (f) are 3D data. The median grain size (Med) is displayed in each histogram. ACIGS samples exhibit significantly larger grain sizes compared to CIGS across all methods. The 3D data provides more accurate grain size estimations, highlighting a threefold increase in ACIGS grain size relative to CIGS.

50 in-plane sections across the film thickness, which gives a larger number of grain counts for analysis (figures 2(b) and (e)). Certainly, by this procedure identical grains would be counted repeatedly. Unlike the cross-sectional results in (a) and (d), the median grain size measured in-plane exhibited a more substantial increase, from 0.26 μm (CIGS) to 0.91 μm (ACIGS), approximately 3.5 times. This observation implies that grain growth induced by Ag addition is anisotropic, resulting in a greater expansion in-plane compared to the thickness direction.

Lastly, figures 2(c) and (f) present grain size histograms from the reconstructed 3D grain structures as determined from the equivalent sphere diameters. Here, the median grain size of ACIGS was observed to be approximately 2.3 times larger compared to CIGS. When comparing the grain sizes obtained from 2D in-plane and 3D analyses, the difference was more pronounced in ACIGS than in CIGS. For ACIGS, the in-plane grain size was approximately 1.6 times larger than the 3D value while for CIGS this factor is close to 1. Moreover, the grain size distributions derived from the 3D reconstructions appeared narrower than those from both 2D analyses. Assuming a lognormal distribution, this narrower histogram shape implies a smaller variance [48, 49]. This occurs because in thin films containing grains of varying sizes, larger grains are frequently observed multiple times in 2D analyses (if the same grains are sectioned repeatedly), whereas in 3D analyses, they are uniquely identified as individual grains. Even in the simplified case of isotropic spherical grains with uniform size, 2D cross-sectional analyses typically underestimate the actual grain size by a factor of approximately πR/4 (figure S2 (a)). For anisotropic structures and samples comprising various grain sizes, these differences can be even larger, emphasizing the difficulty in accurately determining grain sizes from simple 2D measurements (figure S2 (b)).

While the grain statistics in figure 2 were based on equivalent circle or sphere data, the specific grain shape information is not included. This limitation is particularly critical in analysing complex microstructures, such as those found in the CIGS sample, which contains approximately 500 grains. Due to the large number of grains, visualizing each grain individually in three dimensions is impractical. Moreover, selecting only few, specific grains for the analysis may not appropriately represent all grains in a layer. To address this issue, a virtual average grain was generated. Because of different grain position and size, averaging is easier to be performed in k-space than in real-space. Using all grain data, each grain was transformed into frequency-domain data through Fourier transformation:

$$F_n\left(k_x,k_y,k_z\right)=\int\int\int f_n\left(x,y,z\right)\ \exp\left(-2\pi\,\mathrm{i}\left(k_x x+k_y y+k_z z\right)\right)\mathrm{d}x\mathrm{d}y\mathrm{d}z. \tag{1}$$

Here, $f_n(x,y,z)$ is an indicator function that equals 1 inside the nth grain and 0 otherwise. Subsequently, the transformed signal data F_n was summed up and averaged according to equation (2). During this process,

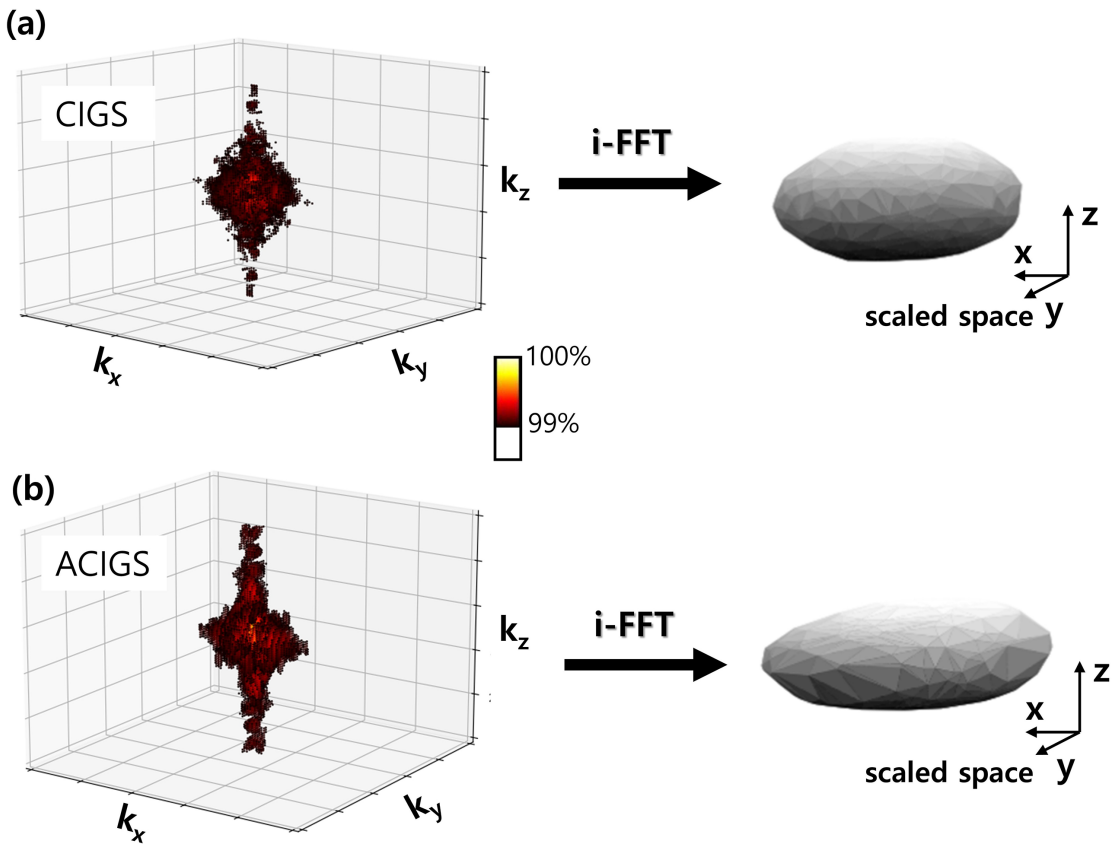

Figure 3. FFT signals and reconstructed grain shapes for CIGS (a) and ACIGS (b). The left graph shows the top 1% magnitude of the averaged FFT signals from all grains measured in each film. The right image presents the reconstructed grain obtained via inverse FFT (i-FFT). The flatter shape observed in ACIGS indicates enhanced growth along the x- and y-axes due to z-axis constraints imposed by the thin-film thickness.

all grains were normalized to the same maximum diameter of each grain (maximum distance between with indicator function value of 1 within one grain) to eliminate the influence of grain size, retaining only the morphological information. The result of this procedure is the function $\bar{F}\left(k_x, k_y, k_z\right)$

$$\bar{F}\left(k_x, k_y, k_z\right) = \frac{1}{N}\sum_{n=1}^{N} F_n\left(k_x, k_y, k_z\right). \tag{2}$$

The left panels in figure 3 visualize the average spectrum obtained after the 3D Fourier transformation. More precise, these panels represent the magnitude (intensity) of the k-space spectrum, converted into a logarithmic scale using $\log\left(\sqrt{\left(\mathrm{Re}(\bar{F})^2 + \mathrm{Im}(\bar{F})^2\right)} + 1\right)$. In order to visualize, we display only the top 1% of the spectrum intensity (see colour code). We see that for ACIGS, the signals in the 1% topmost magnitude range are more elongated along the k_z-direction than in the k_x and k_y direction. This is in distinct difference to the CIGS sample which shows less clear z elongation. Next, based on the averaged signal an inverse fast Fourier transform (i-FFT) was performed using the following equation

$$f'\left(x, y, z\right) = \int\int\int \bar{F}\left(k_x, k_y, k_z\right) \exp\left(2\pi i\left(k_x x + k_y y + k_z z\right)\right) \mathrm{d}k_x \mathrm{d}k_y \mathrm{d}k_z. \tag{3}$$

This results for each sample in a virtual average grain that represent the average grain shape in real space. The virtual average grain images presented in figures 3(a) and (b) demonstrate a tendency for the grains to become flatter upon the addition of Ag. This explains why the discrepancy in grain size between the 2D in-plane and 3D analysis is more pronounced in ACIGS compared to CIGS. The ACIGS grains are larger in x- and y-direction than in z-direction having a disk size. Therefore, the grain size if evaluated by multiple EBSD in-plane sections is becomes overestimated. This morphology of the ACIGS sample is attributed to the limitation in sample thickness, which suppresses growth along the z-axis while promoting more significant expansion in the x and y directions, even though grain growth in principle would be possible in all directions due to Ag addition. This trend is expected to persist in thin films with a thickness of approximately 3 μm.

Table 1. Comparison of grain boundary characteristics between CIGS and ACIGS. The table includes grain boundary densities from 3D evaluation, NGBD: nearest grain boundary distances (average) for 2D and 3D, and twin boundary ratios, which represent the proportion of twin boundaries relative to the total grain boundaries (3D).

	CIGS	ACIGS
Grain boundary density from 3D ($\mu m^2/\mu m^3$)	1.04	0.51
Average NGBD 2D (μm)	0.15	0.55
Average NGBD 3D (μm)	0.12	0.40
Twin boundary ratio 3D (%)	16	19

3.2. Grain boundary analysis

The shape and size of grains also affect their boundaries. Since grain size measurements can vary depending on the used method, the information related to GBs may also differ. We note that only 3D EBSD data cubes are able to provide the grain-boundary orientations throughout the analysed thin film (from 2D EBSD maps, only the trace of a grain boundary can be estimated, and not any information can be obtained on the curvature or connectivity, such as the overall 3D geometry of the grain boundary plane). To gain a deeper understanding of the differences arising from 2D and 3D measurement methods, this study analysed the GBs of CIGS and ACIGS samples using both approaches (table 1).

For a fair comparison, the 3D structures were constructed by stacking individual 2D slices without connecting the GBs along the z-axis, thus, preserving the one-dimensional representation of GBs as in 2D (figure S3). Although in a real 3D microstructure, GBs form continuous surfaces, our approach treats them as lines, resulting in open boundaries at the top and at the bottom of the layer. The CIGS and ACIGS thin films were then analysed separately. According to the results in table 1, the ACIGS sample with Ag addition exhibited a lower grain-boundary density 3D as compared with CIGS. This is simply because of the larger median grain size of ACIGS. On the other hand, we found that the fraction of twin boundaries (with respect to the total density of GBs) in the ACIGS layer is larger than in the CIGS layer. This trend was also found in ACIGS and CIGS layers with different GGI (table S1). This result can be explained by different mechanisms for the reduction of microstrain in the thin films. For layers with large grains reduction of microstrain is realized preferentially via twinning [50]. For layers with small grains (and correspondingly high densities of GBs) microstrain is reduced via relaxation along GBs.

Additionally, to gain a more intuitive understanding of the impact of decreased grain boundary density on charge-carrier recombination, the average, nearest grain-boundary distance (NGBD) was calculated. Because the 3D grain structure data contains a large number of points, calculating all pairwise distances would be computationally inefficient. Therefore, a k–d tree algorithm [51] was implemented to identify the nearest grain boundary for each point. This approach enabled a more than 200-fold improvement in computational speed compared to a brute-force method, allowing for fast and accurate NGBD estimation even in large 3D datasets. Once the nearest grain boundary was identified using the k–d tree, the Euclidean distance from each evaluated point to the closest grain boundary was calculated as

$$||q-x||_2 = \sqrt{\left(\sum_{i=1}^{d}(q_i - x_i)^2\right)}. \tag{4}$$

Here, q represents the reference coordinate, and x denotes the target coordinate being measured.

The results calculated using this method indicate that the average NGBD in ACIGS samples increased by approximately threefold compared to CIGS due to Ag addition. This suggests that the probability of electrons as minority carriers reaching a grain boundary decreases, thereby reducing electron-hole recombination at GBs. These findings serve as a critical indicator for quantitatively explaining the impact of structural changes on the electrical performance of solar cells, based on the correlation between changes in grain size and grain boundary density.

As shown in section 3.1, the grain boundary density and average NGBD also exhibited different results between the 2D and 3D analyses. To ensure a fair comparison between the 2D and 3D data, connections between layers were excluded in the 3D analysis, and the uppermost and lowermost horizontal GBs, which are not detectable in 2D analysis, were also excluded. However, in real thin films, such connections and boundaries do exist, suggesting that the differences between 2D and 3D analyses reported in the present study may be smaller than the actual difference. This issue highlights the inability of 2D analysis to fully capture complex structural characteristics of polycrystalline materials, emphasizing the necessity of 3D modelling for accurate analysis.

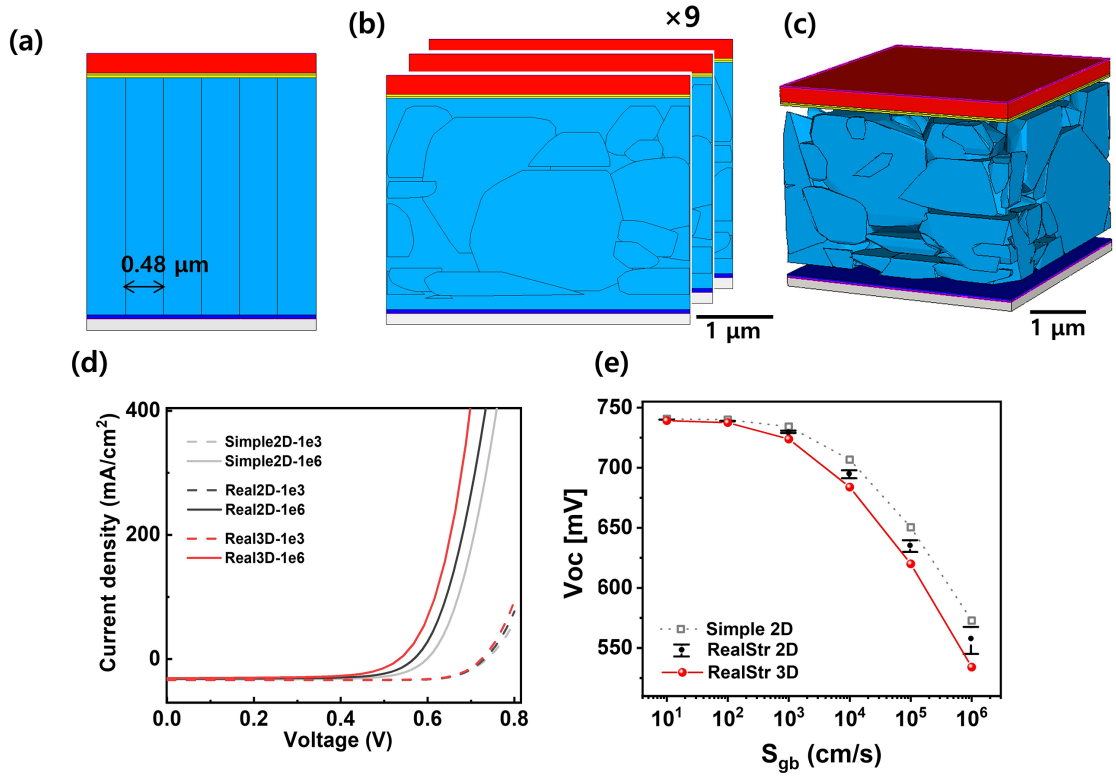

Figure 4. (a) Simplified 2D model with uniform grain boundaries. (b) Realistic 2D model, reconstructed using EBSD data from nine cross-sectional slices. (c) Realistic 3D model, reconstructed using 3D EBSD data, capturing the experimentally determined grain structure. (d) Simulated J–V curves for different models (Simple 2D, one selected Real 2D, and Real 3D) under grain boundary recombination velocities of 10^3 and 10^6 cm s^{-1}. (e) V_{OC} as a function of S_{gb} for each model, showing that 3D models better capture the effects of structural complexity, particularly at high recombination velocities.

3.3. Device simulation results

To evaluate the impact of different spatial dimensions of the analysis methods applied on CIGS and ACIGS absorbers on the simulated photovoltaic performance of corresponding solar cells, the present study constructed an optoelectronic solar-cell model consisting of the absorber layer with two contacts. For the absorber layer model, three configurations were used. The first was a simplified 2D model with GBs running perpendicular to the substrate at 0.48 μm intervals, matching the nearest grain boundary distance of the 3D model (see figure 4(a)). The second was a 2D model based on a grain-boundary grid extracted from a cross-sectional slice of the 3D structure, taking into account grain-size distributions determined at nine different positions (figure 4(b)). The third was a full 3D model incorporating the actual grain structure measured by 3D EBSD (figure 4(c)). The reconstruction process of the real 3D model follows methodologies established in a previous study [41].

Before conducting the 2D and 3D simulations, several electronic material parameters were determined by fitting multiple experimental datasets—such as *J–V*, TRPL, EQE, and CV—using a 1D solar-cell model [52]. Iterative fitting of the experimental data was performed simultaneously using the Nelder–Mead and Levenberg–Marquardt–Gauss algorithms. Subsequently, key parameters such as doping density, effective carrier lifetime, mobility, and conduction band offset derived from the 1D fitting were applied equally to simulate both the 2D and the 3D models (figure S4 and table S2). Using the Sentaurus TCAD software, the Poisson and continuity equations for each model were numerically solved, and *J–V* curves were simulated under standard AM1.5 G conditions. From these simulations, the photovoltaic parameters V_{OC}, J_{SC}, FF, and PCE were derived by analysing the calculated *J–V* curves based on a given recombination velocity at the GBs. Under a short-circuit condition, for which no voltage is applied, the space-charge region (SCR) is rather extended, leading to rather small impact of structural changes at the grain boundary and in the bulk on the charge-carrier collection. In contrast, under an open-circuit condition, the quasi-neutral region becomes wider, while the SCR becomes narrower, making structural changes at the grain boundary and in the bulk more relevant. Indeed, we find clear differences in the simulated V_{OC} values between the models (figure 4(e)), as will be discussed further below.

In case of high grain boundary recombination velocities (e.g. 10^6 cm s^{-1}), the extent of V_{OC} reduction varied significantly among the models. In the simplified 2D model, the decrease was less significant, while in

Table 2. Photovoltaic performance parameters of CIGS and ACIGS solar cells, including V_{OC}, J_{SC}, fill factor (FF) and power conversion efficiency (PCE), as determined from experimental *J–V* curves. The PCE and V_{OC} of ACIGS are lower despite its superior grain structure.

	CIGS	ACIGS
V_{OC} (mV)	733	702
J_{SC} (mA cm^{-2})	33.0	32.2
FF (%)	79.0	77.8
PCE (%)	19.1	17.6

the realistic 2D model reflecting actual structures, the decrease was more pronounced. The largest V_{OC} decrease was found when using the 3D model. These results indicate that the effect of GBs tends to be underestimated as the structural complexity of the model is reduced. Therefore, it was confirmed that simulations incorporating 3D structures are valuable for accurately evaluating the structural changes caused by Ag addition and their impact on photovoltaic performance.

In the previous section, it was confirmed that the addition of Ag significantly increases the grain size of CIGS and that these structural changes can affect the electrical properties of solar cells. However, despite the superior grain structure of the actual ACIGS sample used in this study, its efficiency and V_{OC} were lower than those of CIGS, as shown in table 2. Table S3 as well as Figures S4 and S5 give the result of fitting of several electrical and optoelectronic experiments using one-dimensional modelling. The extracted material properties showed distinct differences between the CIGS and ACIGS layers, in particular higher carrier lifetimes of the CIGS cell (table S3). Thus, the two layers exhibit variations not only in the microstructure but also in optoelectronic properties. At this point, we ascribe these variations to differences in the fabrication process rather than to the inherent effect of Ag addition. Other works have shown that Ag incorporation can improve carrier lifetime and reduce recombination by passivizing defects [22, 23]. However, these effects strongly depend on Ag concentration and process conditions, which may account for differing trends reported in the literature. Therefore, to disentangle the structural effects from other varying factors, a controlled simulation approach was required.

To isolate the effect of Ag-induced structural changes on solar cell efficiency while minimizing the influence of other factors, *J–V* simulations were conducted using the two distinct 3D models (CIGS model and ACIGS model) but one identical electronic parameter set, here the one of CIGS. Since fabricating samples that differ only in the Ag content is practically challenging, this approach ensured that the impact of Ag-induced structural modifications was analysed independently, without interference from variations in carrier properties, band-gap energy, or net-doping concentration.

Figure 5(a) shows the *J–V* simulation results using such CIGS and ACIGS device models. In case of a high recombination velocity at the grain boundary (10^6 cm s^{-1}), the V_{OC} of the CIGS solar cell was found to be smaller than for the ACIGS device. In contrast, the J_{SC} was similar for both solar cells. Again, this result can be attributed to the collection in the SCR being influenced only slightly by changes in the grain boundary properties. Figure 5(b) illustrates the difference in V_{OC} between CIGS and ACIGS as the grain boundary recombination velocity increases. As expected, the V_{OC} increase due to structural changes induced by Ag addition was more pronounced with higher grain boundary recombination velocity S_{gb}. However, this result was derived using carrier lifetime values obtained from one-dimensional fitting, which does not distinguish between bulk and grain boundary effects. Therefore, when considering the actual intra-grain lifetime separately, the resulting minority carrier lifetime is likely higher than the initially set value. As shown by the red symbols in figure 5(b), at a grain boundary recombination velocity of 10^3 cm s^{-1}, which has been reported in [40]., an increase in the intra-grain carrier lifetime by a factor of 2 or even 4 results in a larger V_{OC} gain due to Ag induced structural changes.

While figures 5(a) and (b) present simulation results without considering grain boundary band bending, it has been reported that CIGS GBs exhibit a mixture of upward and downward band bending [6, 40]. Downward band bending acts as hole barrier [53]. In contrast, upward band bending has a relatively minor impact on efficiency compared with downward band bending [5, 54, 55], because it primarily affects minority carriers (electrons), whereas downward band bending impedes the majority carriers (holes) that are crucial for current flow. To simplify the analysis, the present study employed a model assuming only downward band bending at the GBs to calculate the normalized V_{OC} (S_{gb})/V_{OC} (S_{gb} = 10 cm s^{-1}) (figure 5(c)). A band bending value of 30 meV was used [40], and the results were compared with the reference case (effective lifetime from fit and without band bending). The comparison shows that as the recombination velocity at the grain boundary increases, the V_{OC} decreases more gradually. Specifically, when the minority carrier lifetime is high and band bending occurs, the recombination rate at the grain boundary increases, leading to a more pronounced impact on the *V*oc. These results suggest that in absorbers with high

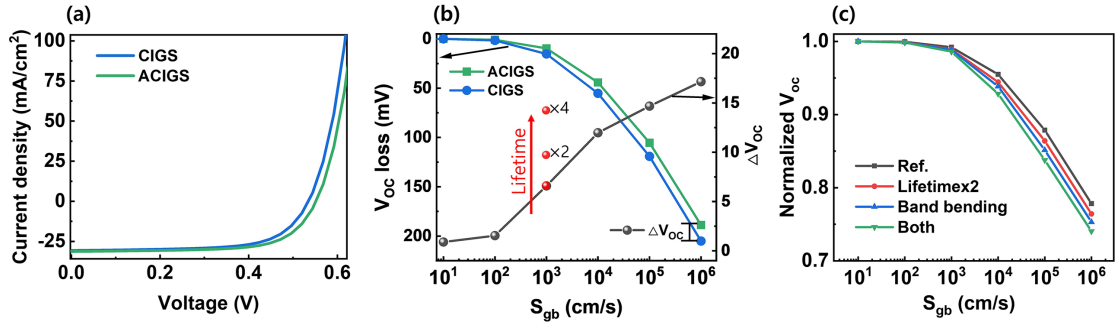

Figure 5. (a) Simulated J–V curves for CIGS and ACIGS for a grain-boundary recombination velocity of 10^6 cm s^{-1} (b) relationship between S_{gb} and V_{OC} loss for CIGS (blue) and ACIGS (green). The black line represents the difference in V_{OC} (ΔV_{OC}) between ACIGS and CIGS as a function of S_{gb}, indicating that higher recombination velocities result in greater V_{OC} for ACIGS compared to CIGS. The red dots illustrate that as the carrier lifetime increases (×2, ×4), the V_{OC} benefit of ACIGS becomes more pronounced. (c) Normalized V_{OC} as a function of S_{gb}, comparing the reference case (black) with scenarios assuming increased carrier lifetime (red), band bending (blue), and both effects combined (green). This indicates that grain boundary recombination has a greater impact on V_{OC} when carrier lifetime increases, band bending occurs, or both effects are combined.

minority carrier lifetimes, the V_{OC} gain due to structural changes is even more significant. This underscores the critical role of the increase in grain size via Ag alloying of CIGS layers for improving the conversion efficiency of the corresponding solar cells.

4. Conclusions

The present study investigated the impact of Ag addition on structural changes in CIGS solar cells using both, 2D and 3D EBSD analyses, and examined how these structural changes influence device performance by means of 3D device simulations. The grain size significantly increased due to Ag addition, as observed in both 2D and 3D analyses, and noticeable differences in grain size and the impact of Ag-induced growth were identified between the 2D in-plane and 3D measurements. The additional benefit of 3D EBSD analysis is to provide the real morphology of individual grains and the orientations of grain-boundary planes in 3D, which are generally inclined. When using real microstructures measured by 2D and 3D EBSD as basis for the 2D and 3D grain-boundary grids used in simulations, it was shown that 2D device simulations somewhat underestimate the impact of grain-boundary recombination on the device performance. The electronic properties of both cells have been extracted from 1D device simulation and appeared to be different beyond the structural differences. The impact of grain boundary recombination velocity has been assessed by using artificially identical electronic properties. The present work highlights the necessity of 3D microstructural analysis and corresponding device simulations for the enhanced understanding of microstructure-property relationships in polycrystalline solar cells.

Data availability statement

All data that support the findings of this study are included within the article (and any supplementary files).

Acknowledgments

This work has received funding from the European Union's Horizon Europe research and innovation program under Grant Agreement No. 101122203 (project Hi-BITS).

The authors are grateful to Ulrike Bloeck (HZB) for assistance with the cross-sectional specimen preparation for SEM. The present work was supported in part by the project 'EFFCIS II' funded by the German Federal Ministry for Economic Affairs and Climate Action (BMWK) under Contract Numbers 03EE1059A (ZSW), 03EE1059B (HZB), and 03EE1059C (MLU).

This work was supported by the Henry Royce Institute for Advanced Materials, funded through EPSRC Grants EP/R00661X/1, EP/S019367/1, EP/P025021/1 and EP/P025498/1, where the 3D EBSD data was gathered using facilities at Henry Royce Institute.

Views and opinions expressed are however those of the author(s) only and do not necessarily reflect those of the European Union. Neither the European Union nor the granting authority can be held responsible for them.

ORCID iDs

Chang-Yun Song https://orcid.org/0000-0002-9132-6844
Zelong Wang https://orcid.org/0009-0004-6056-4868
Heiko Kempa https://orcid.org/0000-0003-3583-6935
Julia Horstmann https://orcid.org/0000-0003-2293-4085
Wolfram Witte https://orcid.org/0000-0002-9429-506X
Rico Gutzler https://orcid.org/0000-0002-1300-6941
Dimitrios Hariskos https://orcid.org/0000-0003-4867-1578
Daniel Abou-Ras https://orcid.org/0000-0003-3063-922X
Roland Scheer https://orcid.org/0000-0001-5007-3425
Ali Gholinia https://orcid.org/0000-0002-2633-133X

References

[1] Shafarman W N, Siebentritt S and Stolt L 2011 $Cu(InGa)Se_2$ Solar Cells *Handbook of Photovoltaic Science and Engineering* (Wiley) pp 546–99
[2] Theelen M and Daume F 2016 Stability of $Cu(In,Ga)Se_2$ solar cells: a literature review *Sol. Energy* **133** 586–627
[3] Keller J, Kiselman K, Donzel-Gargand O, Martin N M, Babucci M, Lundberg O, Wallin E, Stolt L and Edoff M 2024 High-concentration silver alloying and steep back-contact gallium grading enabling copper indium gallium selenide solar cell with 23.6% efficiency *Nat. Energy* **9** 467–78
[4] Gu Y, Zhou C, Chen W, Zhang Y, Yao Y, Zhou Z, Sun Y and Liu W 2024 Silver (Ag) substitution in $Cu(In,Ga)Se_2$ solar cell: insights into current challenges and future prospects *Appl. Phys. A* **130** 636
[5] Cojocaru-Mirédin O, Raghuwanshi M, Wuerz R and Sadewasser S 2021 Grain boundaries in $Cu(In, Ga)Se_2$: a review of composition–electronic property relationships by atom probe tomography and correlative microscopy *Adv. Funct. Mater.* **31** 2103119
[6] Quirk J, Rothmann M, Li W, Abou-Ras D and McKenna K P 2024 Grain boundaries in polycrystalline materials for energy applications: first principles modeling and electron microscopy *Appl. Phys. Rev.* **11** 011308
[7] Gloeckler M, Sites J R and Metzger W K 2005 Grain-boundary recombination in Cu (In,Ga) Se_2 solar cells *J. Appl. Phys.* **98** 113704
[8] Xu M *et al* 2025 16.48% efficient solution-processed CIGS solar cells with crystal growth and defects engineering enabled by Ag doping strategy *J. Energy Chem.* **100** 59–65
[9] Wang C, Zhuang D, Zhao M, Li Y, Dong L, Wang H, Wei J and Gong Q 2022 Effects of silver-doping on properties of $Cu(In,Ga)Se_2$ films prepared by CuInGa precursors *J. Energy Chem.* **66** 218–25
[10] Gutzler R, Witte W, Kanevce A, Hariskos D and Paetel S 2023 VOC-losses across the band gap: insights from a high-throughput inline process for CIGS solar cells *Prog. Photovolt.: Res. Appl.* **31** 1023–31
[11] Kim G, Kim W M, Park J K, Kim D, Yu H and Jeong J H 2019 Thin Ag precursor layer-assisted co-evaporation process for low-temperature growth of $Cu(In,Ga)Se_2$ thin film *ACS Appl. Mater. Interfaces* **11** 31923–33
[12] Keller J, Stolt L, Sopiha K V, Larsen J K, Riekehr L and Edoff M 2020 On the paramount role of absorber stoichiometry in $(Ag,Cu)(In,Ga)Se_2$ wide-gap solar cells *Sol. RRL* **4** 2000508
[13] Keller J, Pearson P, Shariati Nilsson N, Stolt O, Stolt L and Edoff M 2021 Performance limitations of wide-gap $(Ag,Cu)(In,Ga)Se_2$ thin-film solar cells *Sol. RRL* **5** 2100403
[14] Calderón E, Fernández B, Durán L, Grima P, Morocoima M, Quintero E, Rincón C and Quintero M 2009 Temperature variation of the fundamental absorption edge in $AgGaSe_2$ *Physica B* **404** 4095–9
[15] Sharan A, Sabino F P, Janotti A, Gaillard N, Ogitsu T and Varley J B 2020 Assessing the roles of Cu- And Ag-deficient layers in chalcopyrite-based solar cells through first principles calculations *J. Appl. Phys.* **127** 065303
[16] Keller J, Sopiha K V, Stolt O, Stolt L, Persson C, Scragg J J S, Törndahl T and Edoff M 2020 Wide-gap $(Ag,Cu)(In,Ga)Se_2$ solar cells with different buffer materials—A path to a better heterojunction *Prog. Photovolt.: Res. Appl.* **28** 237–50
[17] Larsen J K, Donzel-Gargand O, Sopiha K V, Keller J, Lindgren K, Platzer-Bjorkman C and Edoff M 2021 Investigation of $AgGaSe_2$as a wide gap solar cell Absorber *ACS Appl. Energy Mater.* **4** 1805–14
[18] Kim K *et al* 2018 Highly efficient Ag-alloyed $Cu(In,Ga)Se_2$ solar cells with wide bandgaps and their application to chalcopyrite-based tandem solar cells *Nano Energy* **48** 345–52
[19] Erslev P T, Lee J, Hanket G M, Shafarman W N and Cohen J D 2011 The electronic structure of $Cu(In_{1-x}Ga_x)Se_2$ alloyed with silver *Thin Solid Films* **519** 7296–9
[20] Falk H H, Eckner S, Ritter K, Levcenko S, Pfeiffelmann T, Larsen J, Shafarman W N and Schnohr C S 2025 Driving factors for the peculiar bond length dependence and tetragonal distortion of $(Ag,Cu)(In,Ga)Se_2$ and other chalcopyrites *J. Phys. Energy* **7** 1
[21] Zhang Y *et al* 2021 Silver-assisted optimization of band gap gradient structure of $Cu(In,Ga)Se_2$ solar cells via SCAPS *Sol. Energy* **227** 334–42
[22] Kanevce A, Essig S, Paetel S, Hempel W, Hariskos D and Magorian Friedlmeier T 2022 Impact of Ag content on device properties of $Cu(In,Ga)Se_2$ solar cells *EPJ Photovolt.* **13** 28
[23] Mori H, Chantana J, Kawano Y, Negami T and Minemoto T 2023 Influence of silver introduction into $(Ag,Cu)(In,Ga)S_2$ thin films on their physical properties *Mater. Sci. Eng. B* **297** 116758
[24] Stechmann G, Zaefferer S, Konijnenberg P, Raabe D, Gretener C, Kranz L, Perrenoud J, Buecheler S and Tiwari A N 2016 3-Dimensional microstructural characterization of CdTe absorber layers from CdTe/CdS thin film solar cells *Sol. Energy Mater. Sol. Cells* **151** 66–80
[25] Krause M *et al* 2020 Microscopic origins of performance losses in highly efficient $Cu(In,Ga)Se_2$ thin-film solar cells *Nat. Commun.* **11** 4189
[26] Park H K, Yim K, Lee J, Cho Y, Jeong I, Shin D, Gwak J, Walsh A, Kim K and Jo W 2024 Interplay between strain and charge in $Cu(In,Ga)Se_2$ flexible photovoltaics *npj Flex. Electron.* **8** 58
[27] Yao Y, Ma J, Liu Y, Yang X, Meng H, Liu F, Zhang Y and Liu W 2025 Achieving over 860 mV open-circuit voltage in low-ag wide-bandgap $Cu(In,Ga)Se_2$ solar cells through ion diffusion and band structure optimization *Adv. Funct. Mater.* 2423228

[28] Zhang J et al 2024 Highly efficient narrow bandgap Cu(In,Ga)Se_2 solar cells with enhanced open circuit voltage for tandem application *Nat. Commun.* **15** 10365
[29] Gabor A M, Tuttle J R, Albin D S, Contreras M A, Noufi R and Hermann A M 1994 High-efficiency $CuIn_xGa_{1-x}Se_2$ solar cells made from $(In_x,Ga_{1-x})_2Se_3$ precursor films *Appl. Phys. Lett.* **65** 198–200
[30] Gabor A M, Tuttle J R, Bode M H, Franz A, Tennant A L, Contreras M A, Noufi R, Jensen D G and Hermann A M 1996 Band-gap engineering in Cu(In,Ga) Se_2 thin films grown from $(In,Ga)_2Se_3$ precursors *Sol. Energy Mater. Sol. Cells* **41** 247–60
[31] Jackson P, Wuerz R, Hariskos D, Lotter E, Witte W and Powalla M 2016 Effects of heavy alkali elements in Cu(In,Ga)Se_2 solar cells with efficiencies up to 22.6% *Phys. Status Solidi—Rapid Res. Lett.* **10** 583–6
[32] Burnett T L, Kelley R, Winiarski B, Contreras L, Daly M, Gholinia A, Burke M G and Withers P J 2016 Large volume serial section tomography by Xe Plasma FIB dual beam microscopy *Ultramicroscopy* **161** 119–29
[33] Gholinia A, Brough I, Humphreys J and Bate P 2012 A 3D FIB investigation of dynamic recrystallization in a Cu-Sn bronze *Materials Science Forum* vol 715–716 (Trans Tech Publications Ltd.) pp 498–501
[34] Jangid D K, Brodnik N R, Echlin M L P, Gudavalli C, Levenson C, Pollock T M, Daly S H and Manjunath B S 2024 Q-RBSA: high-resolution 3D EBSD map generation using an efficient quaternion transformer network *npj Comput. Mater* **10** 27
[35] Ider M 2020 Determination of the gibbs formation energy of $CuGaSe_2$ by EMF method *Int. J. Electrochem. Sci.* **15** 9049–65
[36] Kim W K, Payzant E A, Kim S, Speakman S A, Crisalle O D and Anderson T J 2008 Reaction kinetics of $CuGaSe_2$ formation from a GaSe/CuSe bilayer precursor film *J. Cryst. Growth* **310** 2987–94
[37] Cahen D and Noufi R 1992 Free energies and enthalpies of possible gas phase and surface reactions for preparation of $cuinse_2$ *J. Phys. Chem. Solids* **53** 991–1005
[38] Balboul M R, Schock H W, Fayak S A, El-Aal A A, Werner J H and Ramadan A A 2008 Correlation of structure parameters of absorber layer with efficiency of Cu(In,Ga)Se_2 solar cell *Appl. Phys. A* **92** 557–63
[39] Abou-Ras D, Caballero R, Kaufmann C A, Nichterwitz M, Sakurai K, Schorr S, Unold T and Schock H W 2008 Impact of the Ga concentration on the microstructure of $Culn_{1-x}$ Gax Se_2 *Phys. Status Solidi—Rapid Res. Lett.* **2** 135–7
[40] Thomas S, Witte W, Hariskos D, Paetel S, Song C Y, Kempa H, Maiberg M, El-Ganainy N and Abou-Ras D 2024 Effect of Ga variation on the bulk and grain-boundary properties of Cu(In,Ga)Se_2 absorbers in thin-film solar cells and their impacts on open-circuit voltage losses *Prog. Photovolt.: Res. Appl.* **33** 265–75
[41] Song C Y, Maiberg M, Kempa H, Witte W, Hariskos D, Abou-Ras D, Moeller B, Scheer R and Gholinia A 2024 A new approach to three-dimensional microstructure reconstruction of a polycrystalline solar cell using high-efficiency Cu(In,Ga)Se_2 *Sci. Rep.* **14** 2036
[42] Knight K S 1992 The crystal structures of $CuInSe_2$ and $CuInTe_2$ **27** 161–7
[43] Couzinié-Devy F, Barreau N and Kessler J 2011 Re-investigation of preferential orientation of Cu(In,Ga)Se_2 thin films grown by the three-stage process *Prog. Photovolt.: Res. Appl.* **19** 527–36
[44] Kim N and Martin P P Rockett A A and Ertekin E 2016 Screened-exchange density functional theory description of the electronic structure and phase stability of the chalcopyrite materials AgInSe2 and AuInSe2 *Phys. Rev. B* **93** 165202
[45] Thomas S, Witte W, Hariskos D, Gutzler R, Paetel S, Song C Y, Kempa H, Maiberg M and Abou-Ras D 2024 Role of ag addition on the microscopic material properties of (Ag,Cu)(In,Ga)Se_2 absorbers and their effects on losses in the open-circuit voltage of corresponding devices *Prog. Photovolt.: Res. Appl.* **32** 930–40
[46] Sun Z, Tsai S-P, Konijnenberg P, Wang J-Y and Zaefferer S 2024 A large-volume 3D EBSD study on additively manufactured 316L stainless steel *Scr. Mater.* **238** 115723
[47] Cooperdock E H G, Ketcham R A and Stockli D F 2019 Resolving the effects of 2-D versus 3-D grain measurements on apatite (U-Th)/He age data and reproducibility *Geochronology* **1** 17–41
[48] Frost H J, Thompson C V and Walton D T 1990 Simulation of thin film grain structures-I. grain growth stagnation *Acta Metall. Mater.* **38** 1455–62
[49] Yang S, Song Q, Chao L, Li D and Wang Y 2024 Grain characteristics of perovskite thin films based on SEM image segmentation *Adv. Theor. Simul.* **7** 2300619
[50] Simoes S, Calinas R, Vieira M T, Vieira M F and Ferreira P J 2010 In situ TEM study of grain growth in nanocrystalline copper thin films *Nanotechnology* **21** 145701
[51] Friedman J H, Louis Bentley J, Ari Finkel R and Frmdman J 1977 An algorithm fqr finding best in logarithmic expected time *ACM Trans. Math. Softw.* **3** 209–26
[52] Maiberg M, Song C-Y, Morawski M, Neduck F, Kempa H, Damm J, Hariskos D, Witte W and Scheer R 2024 Toward digital twins by one-dimensional simulation of thin-film solar cells: cu(In,Ga)Se_2 as an example *Phys. Rev. Appl.* **21** 034051
[53] Gaury B and Haney P M 2017 Charged grain boundaries and carrier recombination in polycrystalline Thin-Film solar cells *Phys. Rev. Appl.* **8** 054026
[54] Nicoara N, Manaligod R, Jackson P, Hariskos D, Witte W and Sozzi G Menozzi R and Sadewasser S 2019 Direct evidence for grain boundary passivation in Cu(In,Ga)Se_2 solar cells through alkali-fluoride post-deposition treatments *Nat. Commun.* **10** 3980
[55] Prabu R T, Malathi S R, Kumar R, Alkhalidi H S and Kumar A 2024 Impact of grain size and grain nature in thin-film solar cells *Energy Technol.* **12** 2300754